Boundary-Layer Meteorol (2009) 130:229–247
DOI 10.1007/s10546-008-9340-8

ORIGINAL PAPER

A Lagrangian Stochastic Model for Heavy Particle Dispersion in the Atmospheric Marine Boundary Layer

James A. Mueller · Fabrice Veron

Received: 20 December 2007 / Accepted: 24 November 2008 / Published online: 11 December 2008

Abstract The dispersion of heavy particles and pollutants is often simulated with Lagrangian stochastic (LS) models. Although these models have been employed successfully over land, the free surface at the air-sea interface complicates the implementation of traditional LS models. We present an adaptation of traditional LS models to the atmospheric marine boundary layer (MBL), where the bottom boundary is represented by a realistic wavy surface that moves and deforms. In addition, the correlation function for the turbulent flow following a particle is extended to the anisotropic, unsteady case. Our new model reproduces behaviour for Lagrangian turbulence in a stratified air flow that departs only slightly from the expected behaviour in isotropic turbulence. When solving for the trajectory of a heavy particle in the air flow, the modelled turbulent forcing on the particle also behaves remarkably well. For example, the spectrum of the turbulence at the particle location follows that of a massless particle for time scales approximately larger than the Stokes' particle response time. We anticipate that this model will prove especially useful in the context of sea-spray dispersion and its associated momentum, sensible and latent heat, and gas fluxes between spray droplets and the atmosphere.

Keywords Heavy particle dispersion · Lagrangian stochastic model · Marine boundary layer · Multiphase flow · Sea spray · Wave-induced stress

1 Introduction

The study of small particle dispersion in any boundary layer inherently involves the study of turbulence, as molecular diffusion is orders of magnitude smaller than turbulent diffusion.

J. A. Mueller (✉) · F. Veron
College of Marine and Earth Studies, University of Delaware,
112C Robinson Hall, Newark, DE 19716, USA
e-mail: jmueller@udel.edu

F. Veron
e-mail: fveron@udel.edu

Because direct numerical simulation techniques are too computationally expensive for most applications, including the one presented here, the turbulent flow needs to be modelled. Different turbulence models have various strengths and weaknesses, and the results can be sensitive to the model that is used. For this study, we choose to use a Lagrangian turbulence model. Although Lagrangian coordinates, which follow the trajectories of individual fluid parcels, are sometimes more physically intuitive in describing fluid motion than Eulerian coordinates that are fixed in space, Lagrangian coordinates are used less frequently because they are often awkward to implement. Studies of particle dispersion and mixing, however, are well-suited for a Lagrangian frame of reference (Yeung 2002), and modern computing power has enabled the calculation of the large number of random trajectories necessary for Lagrangian stochastic (LS) modelling. A primary advantage is the superior accuracy of dispersion simulation in the near field of a source. In the atmospheric boundary layer, LS models have successfully captured the paths of particles with only a crude knowledge of the turbulent flow, i.e. using only the low-order velocity statistics (Wilson and Sawford 1996). LS models have also been coupled with large-eddy simulations (LES) of the planetary boundary layer (Weil et al. 2004); the extension to LES, however, is beyond the scope of this paper. Naturally, the complex geometry inherent in the atmosphere marine boundary layer (MBL) makes LS modelling especially appealing for studies of particle dispersion; recently, LS modelling has recently been used in the coastal ocean boundary layer (Brickman and Smith 2002).

The turbulence, and in particular the turbulent stress, within the MBL differs substantially from that over a flat, solid, stationary boundary. The introduction of a moving, wavy, bottom boundary causes the surface stress to become a function of the sea state. The vertical profiles of stress components and velocity also change. In addition to the viscous, logarithmic, and defect layers, a wave boundary layer forms (WBL). Like the viscous layer, the WBL reduces the turbulent fraction of the stress near the surface, but by the top of the inner region of the WBL, the turbulent component carries nearly all of the stress. The depth of this layer depends on the length scales of the wave field but is generally greater than the depth of the viscous layer. Therefore, within the marine boundary, the local turbulent stress changes with height above the surface, producing local inhomogeneities in both the horizontal and vertical directions.

Often the dispersive particles of interest are not fluid parcels or passive tracers but rather discrete elements with different material properties from the carrier fluid. When the density of the particle differs significantly from that of the carrier fluid, the particle no longer follows the fluid flow field due to its non-negligible inertia and relative gravitational force. In response to numerous geophysical and engineering applications, the statistics of heavy particle motion has been studied extensively (e.g. Yudine 1959; Csanady 1963; Snyder and Lumley 1971; Reeks 1977; Wells and Stock 1983; Wang and Maxey 1993). An advantage of LS models for heavy particle dispersion is the ability to include temporal evolution of the particle phase, such as droplet evaporation, with relative ease. An important setback, however, is the difficulty involved in the trajectory calculation of the heavy particle. The fluid velocity that drives the heavy particle motion does not follow a fluid Lagrangian velocity sequence or an Eulerian velocity field. Therefore, a hybrid of the Eulerian and Lagrangian (spatial and temporal) frames of reference must be formulated for models of heavy particle dispersion. This will be discussed in Sect. 4. Before considering heavy particle transport in the MBL, the velocity structure and turbulence of the carrier fluid (air) will be presented in the next section.

2 Air Velocity

To model the instantaneous velocity of the air flow in the MBL and above a wavy surface, we use the standard Reynolds decomposition where the velocity of the air, $\mathbf{u}$, is represented by:

$$\mathbf{u} = \overline{\mathbf{U}} + \mathbf{u}''. \tag{1}$$

Here $\overline{\mathbf{U}}$ is the ensemble or temporal average in surface-following coordinates, and $\mathbf{u}''$ is the turbulent deviation from the mean that can be further decomposed into phase coherent and incoherent components, respectively:

$$\mathbf{u}'' = \widetilde{\mathbf{u}} + \mathbf{u}'. \tag{2}$$

The total phase coherent component of the instantaneous velocity is denoted $\mathbf{U} = \overline{\mathbf{U}} + \widetilde{\mathbf{u}}$ so that $\mathbf{u} = \mathbf{U} + \mathbf{u}'$. We first consider this mean air velocity.

2.1 Eulerian Mean and Wave Phase-Locked Velocity

The mean velocity field is one of the parameters that must be known for LS models. Turbulent boundary-layer theory over a smooth flat surface offers a starting point for the velocity profile over ocean waves. Within a turbulent boundary layer, three distinct regions form. The first region closest to the surface is the viscous sublayer, where molecular forces dominate. The velocity profile in this layer is linear. The second region is the log layer, where the turbulent stresses dominate and the velocity profile becomes logarithmic in neutrally stratified conditions. In smooth flow, these two regions, the viscous sublayer and the log layer, are self-similar in wall coordinates (i.e. normalized distance from the wall $z^+ = zu_*/\nu$ and normalized mean velocity $U^+ = \overline{U}/u_*$, where u_* is the friction velocity and ν is the kinematic viscosity of the air). The third region is the defect layer, where the profile is not self-similar. In the MBL, waves form, grow, and interact. Small capillary waves effectively cause the surface to become rougher, and surface gravity waves make the surface hilly. In addition, the waves propagate at different phase speeds. Therefore, the velocity profile over ocean waves, not surprisingly, departs from the smooth, flat plate case.

Before proceeding to the air velocity field, the wavy bottom boundary needs to be considered. In fact, the presence of this complex bottom boundary creates rich features in the air flow that distinguish this study from previous LS model applications and will be presented in subsequent sections. The amplitudes of capillary and deep-water gravity wave modes, a_n, follow the empirical omnidirectional spectrum of Elfouhaily et al. (1997) and are linearly superposed. Consequently, the instantaneous elevation of the surface becomes:

$$\eta(x,t) = \sum_n a_n \cos\left(k_n x - \omega_n t + \phi_n\right), \tag{3}$$

where k_n, ω_n, and ϕ_n are the wavenumber, orbital frequency, and phase of each wave mode n respectively. The phase speed of each wave mode is $c_n = \omega_n/k_n$, determined by the dispersion relationship for deep-water capillary-gravity waves. Each wave phase, ϕ_n, is chosen from a random distribution uniformly distributed on the interval $[-\pi, \pi)$. In the remainder of this paper, the altitude is referenced to the surface elevation, η, such that the new height is the distance above the local surface, $\zeta(x, z, t) = z - \eta(x, t)$.

Assuming large-scale steady flow with no pressure gradient, conservation of momentum implies a constant stress layer above the surface. In addition to turbulent and viscous stresses present in the flat plate case, there are also wave-induced and separation stresses in the MBL. At low wind speeds, viscous stress dominates the air-sea surface stress, but as the wind speed

increases, however, separation and wave-induced stresses become dominant. The partition of the surface stress is modelled according to Mueller and Veron (2008). The vertical profile of the stress components, however, is the topic of Sect. 3.

The form for the mean horizontal velocity profile is determined using a hybrid of the standard logarithmic profile from flat plate theory and the van Driest damping function (1956), which approximates both the near-wall linear, molecular sublayer and the smooth transition to the log layer. In fact, the mean horizontal velocity profile is simply the summation of the two layers with the logarithmic layer exponentially damped in the near-wall region, as follows (Mueller and Veron 2008):

$$\overline{U}(\zeta) - \overline{U}_0 = 10u_{*_\nu}\left[1 - \exp(-\zeta u_*/10\nu)\right]\frac{u_{*_\nu}}{u_*} + \left[1 - \exp(-\zeta u_*/10\nu)\right]\frac{u_*}{\kappa}\left[\ln\left(\frac{\zeta + D}{D}\right) - \Phi_m\right], \tag{4}$$

where $\kappa = 0.4$ is the von Karman constant, $\rho u_{*_\nu}^2$ represents the viscous component of the surface stress, and ρ denotes the air density; $\overline{U}_0$ is the horizontal surface velocity and is a function of surface viscous stress only and is usually taken to be a fraction of u_{*_ν} (Wu 1983). The stability correction due to stratification is $\Phi_m(\zeta/L)$, which is a function of height and the Obukhov length scale, L. The roughness length, z_0, is introduced such that the logarithmic profile is not singular at the surface, and outside of the viscous layer the profile converges to the standard log profile. The variable D merely ensures a smooth transition between the two layers, regardless of the flow roughness, and is defined in terms of the roughness length:

$$D = z_0 \exp\left(\frac{\kappa 10 u_{*_\nu}^2}{u_*^2}\right). \tag{5}$$

As it follows the surface displacement, the mean horizontal wind profile is shifted up and down. The presence of surface waves further modifies the instantaneous, local wind field however. For one thing, conservation of mass requires an acceleration of the air flow when the surface is above the mean surface level and a deceleration when the surface is below the mean surface level (see Appendix A). Moreover, the presence of a non-flat surface generates a vertical component in the wind speed, as the wind follows the instantaneous surface elevation in order to satisfy the continuity of velocity at the surface. These effects are exponentially damped in the vertical with a decay rate proportional to the local surface wavelength. This is similar to the damping of orbital motion with height. In other words, very close to the undulating surface the wind will be exactly parallel to that surface, and as altitude increases, the wind will follow only the longer-wavelength surface displacements. Eventually, at sufficient heights, the effects of the waves are not "felt" any longer and the mean air velocity is solely in the horizontal direction. In the remainder of the text, we adopt the tensor index notation where $\overline{U}_1 = \overline{U}(\zeta)$ is the mean wind velocity component in the x streamwise direction, $\overline{U}_2$ denotes the mean wind velocity component in the y spanwise direction (not used in this two-dimensional model), and $\overline{U}_3$ is the mean wind velocity component in the ζ vertical direction. In the neutral case, there is no mean vertical velocity, $\overline{U}_3 = 0$. In stratified flows, there is a small, mean vertical velocity known as the Webb correction (Webb et al. 1980; Webb 1982).

The mean horizontal velocity component produces a phase coherent vertical velocity perturbation due to the wavy surface, and for the air flow to follow the wavy surface, this component is

$$U_3^{sur}(\zeta) = \overline{U}_1(\zeta)\alpha = \overline{U}_1(\zeta)\sum_n -a_n k_n \sin(k_n x - \omega_n t + \phi_n)\exp(-k_n\zeta). \tag{6}$$

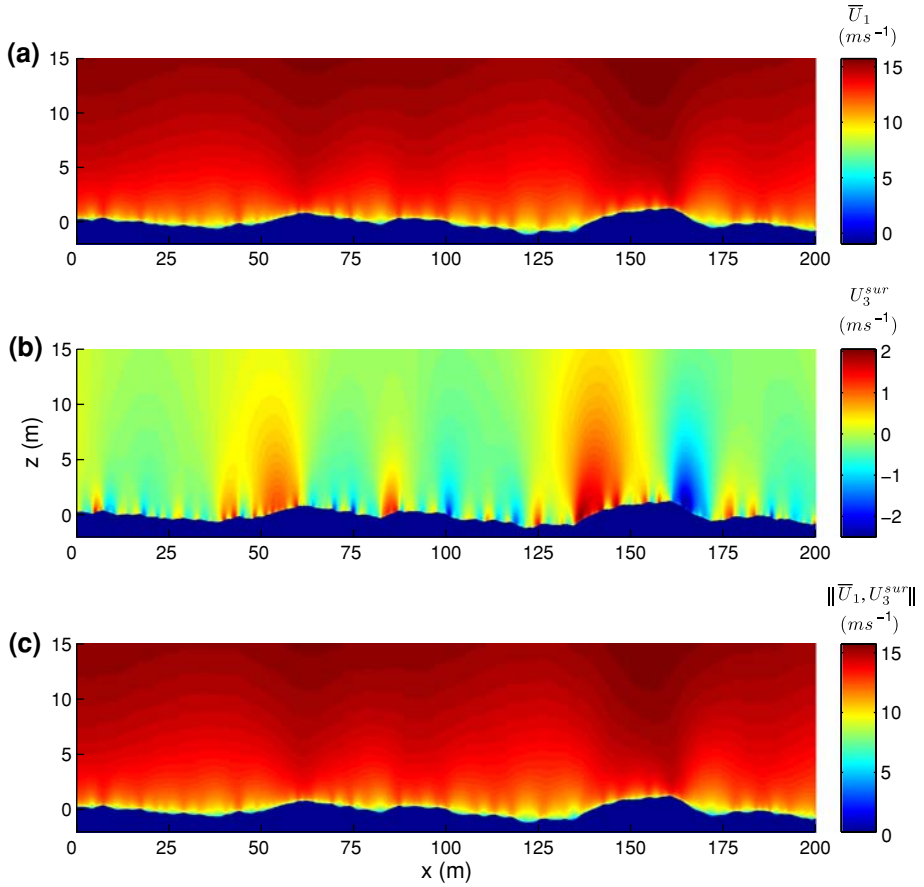

Fig. 1 Horizontal (**a**) and vertical (**b**) velocity components and their norm (**c**) over a sample section of the wave field for a 15 m s^{-1}, 10-m wind speed

Here, α is a factor exactly equal to the surface slope $\partial\eta/\partial x$ at the surface ($\zeta = 0$), and damped with height above the surface proportionally to the local surface wavelength, as explained above. Figure 1 shows the horizontal and vertical velocity, which includes phase dependent acceleration/deceleration (see Appendix A), as well as their Euclidean norm over a section of the wave field. The wave field, determined by the wind-wave equilibrium for a 150-km fetch (see Mueller and Veron 2008), has a dominant wave steepness of $ak \approx 0.11$ and a peak wavenumber of $k_p \approx 0.083$ rad m^{-1}. In Fig. 1a, the acceleration at the crests and deceleration at the troughs are apparent in the respective compression and expansion of the local vertical profiles of $\overline{U}_1(\zeta)$. At 10 m, the velocity is roughly 15 m s^{-1} over the entire wave field; the horizontal velocity satisfies the upper boundary condition as it becomes uniform, to numerical accuracy, with increasing height. In Fig. 1b, the decay of the vertical velocity with increasing height is more apparent. At 15 m, there are only perturbations due to the dominant waves. Finally, Fig. 1c shows that most of the kinetic energy is contained in the horizontal components of the velocity field as expected. The wave-following velocity further illustrates the acceleration and deceleration of the total velocity at the crests and troughs of the waves.

The wind orbital velocity (i.e. the temporal derivative of the particle orbits) induced by the undulation of the surface waves is also part of the total phase coherent velocity field, yielding:

$$U_1(x,\zeta,t) = \overline{U}_1(\zeta) + U_1^{orb}(x,\zeta,t) + U_1^{acc}(x,\zeta,t), \tag{7}$$

$$U_3(x,\zeta,t) = \overline{U}_3(\zeta) + U_3^{orb}(x,\zeta,t) + U_3^{acc}(x,\zeta,t) + U_3^{sur}(x,\zeta,t), \tag{8}$$

where the horizontal and vertical orbital velocities are

$$U_1^{orb}(x,\zeta,t) = \sum_n -a_n\omega_n \cos(k_n x - \omega_n t + \phi_n)\exp(-k_n\zeta), \tag{9}$$

$$U_3^{orb}(x,\zeta,t) = \sum_n a_n\omega_n \sin(k_n x - \omega_n t + \phi_n)\exp(-k_n\zeta). \tag{10}$$

Figure 2 shows the horizontal and vertical orbital velocities over the wave field. At 10 m, only the motions of the dominant waves affect the air flow. With the phase coherent components of the velocity field, the turbulent velocity, $\mathbf{u}'$, can now be modelled. To that end, we choose here to use a Lagrangian stochastic turbulence model that we will further develop for use in non-isotropic, non-homogeneous cases such as those encountered for particle dispersion in the stratified MBL.

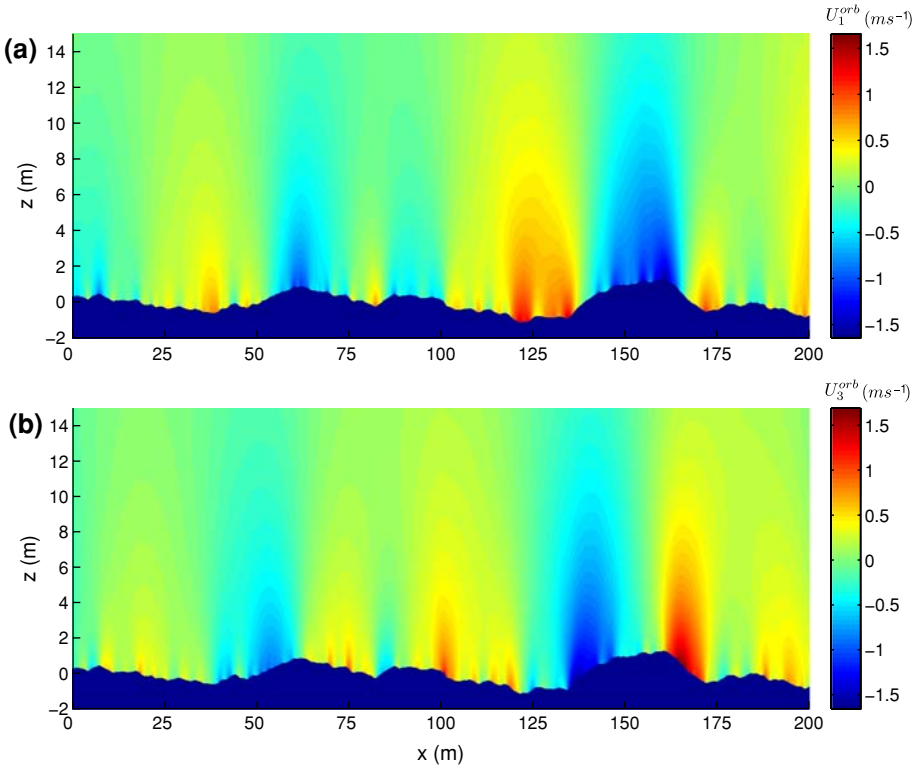

Fig. 2 Horizontal (**a**) and vertical (**b**) orbital velocities over a sample section of the wave field for a 15 m s^{-1}, 10-m wind speed

2.2 Lagrangian Stochastic Turbulence

The underlying principle of LS models is that certain variables of a fluid particle evolve as a Markov process, which means that consecutive values in time are partially correlated and the uncorrelated component is independent of previous values (see Rodean 1996 for a review of LS models). Markov processes are not only well understood mathematically but can also be used to describe the evolution of the position, velocity, and acceleration of a fluid element within a turbulent flow. A zero-order LS model treats the fluid particle position as Markovian, and the random displacement model is recovered. Likewise, a first-order LS model, or originally proposed by Taylor (1921) as the drunkard's walk, treats the fluid particle velocity as Markovian, recovering the generalized Langevin equation (Thomson 1987). Finally, a second-order LS model treats the acceleration as Markovian (Du et al. 1995). We now consider the first-order LS model with Markov state variable, (X_i, u_i'), where X_i and u_i' are the position and turbulent velocity components, respectively.

The generalized Langevin equation is (Thomson 1987):

$$\mathrm{d}u_i = a_i \mathrm{d}t + b_{ij}\mathrm{d}\xi_j, \tag{11}$$

where $u_i = U_i + u_i'$ is the instantaneous velocity and $\mathrm{d}\xi_j$ is an independent Gaussian variable with zero mean and variance $\mathrm{d}t$. Consistency of the Langevin equation with Kolmogorov's second hypothesis (i.e. turbulent statistics in the inertial subrange are independent of viscosity, ν, and are only a function of the mean rate of kinetic energy dissipation) defines a diagonal b_{ij} such that $b_{ij} = \sqrt{C_0\varepsilon}\delta_{ij}$, where C_0 is the Kolmogorov constant from the second-order Lagrangian structure function in the inertial subrange and ε is the mean rate of kinetic energy dissipation (see Appendix B). Thus, when $a_i = -u_i/T_L$, the classical Langevin equation is recovered with the Lagrangian velocity integral time scale, T_L. The classical Langevin equation, however, does not strictly apply to inhomogeneous or non-stationary flows. In fact, Thomson (1987) pointed out that the classical Langevin equation fails to satisfy what he called the "well-mixed criterion," which states that a passive tracer that is initially well-mixed should stay well mixed. But even the imposition of the well-mixed criterion does not yield a unique solution for a_i in multiple dimensions, despite the uniqueness of a for the one-dimensional case (Thomson 1987). Nevertheless, Thomson (1987) proposed the simplest solution, which, in tensor notation with the usual summation convention, becomes:

$$a_i = -\frac{C_0\varepsilon}{2}\hat{\tau}_{ik}^{-1}u_k' + \psi_i, \tag{12}$$

where

$$\psi_i = \frac{\partial U_i}{\partial t} + U_j\frac{\partial U_i}{\partial x_j} + \frac{1}{2}\frac{\partial \hat{\tau}_{ij}}{\partial x_j} + \frac{\hat{\tau}_{im}^{-1}}{2}\frac{\partial \hat{\tau}_{km}}{\partial x_j}u_j'u_k' + \left[\frac{\partial U_i}{\partial x_j} + \frac{\hat{\tau}_{im}^{-1}}{2}\left(\frac{\partial \hat{\tau}_{jm}}{\partial t} + U_k\frac{\partial \hat{\tau}_{jm}}{\partial x_k}\right)\right]u_j', \tag{13}$$

and $\hat{\tau}_{ij}$ is the stress tensor divided by the air density; $\hat{\tau}_{ij}^{-1}$ is the inverse stress tensor; a prime indicates the turbulent component. The first term in a_i is the fading memory term such that, when discretized, there is at each timestep only a partial correlation with the previous step. The second term, ψ_i, is the drift term, which accounts for the inhomogeneity and non-stationarity. We further simplify Eq. 13 using the following assumption: the horizontal inhomogeneity arises from the change of coordinates due to the wavy bottom boundary but

not from the horizontal gradient of the vertical velocity, as this is negligible due to the small wave slope. Also, we only consider the vertical and horizontal directions ($i = \{1, 3\}$) here.

With these assumptions and solving for the turbulent component, Eq. 11 reduces to:

$$\mathrm{d}u_i' = \left(\Psi_i - \frac{C_0\varepsilon}{2}\hat{\tau}_{ik}^{-1}u_k'\right)\mathrm{d}t + b_{ij}\mathrm{d}\xi_j, \tag{14}$$

where

$$\Psi_i = \frac{1}{2}\frac{\partial\hat{\tau}_{ij}}{\partial x_j} + \left[\frac{\hat{\tau}_{im}^{-1}}{2}\left(\frac{\partial\hat{\tau}_{jm}}{\partial t} + U_k\frac{\partial\hat{\tau}_{jm}}{\partial x_k}\right)\right]u_j' + \frac{\hat{\tau}_{im}^{-1}}{2}\frac{\partial\hat{\tau}_{km}}{\partial x_j}u_j'u_k'. \tag{15}$$

In its discretized form, where Δt is the numerical timestep, the turbulent velocity at time $t + \Delta t$ is given by:

$$u_i'(t+\Delta t) = u_i'(t) - (1-R_i)\,\sigma_i^2\hat{\tau}_{ik}^{-1}u_k' + (1-R_i)\,T_{L_i}\Psi_i + \sigma_i\sqrt{1-R_i^2}\gamma, \tag{16}$$

where σ_i^2 is the variance of the ith turbulent velocity component, $R_i = \exp(-\Delta t/T_{L_i})$ is the autocorrelation of the ith component, and $T_{L_i} = 2\sigma_i^2/C_0\varepsilon$ is the local Lagrangian integral time scale. Also, γ is an independent Gaussian variable with zero mean and unit variance. The components of the inverse stress tensor, $\hat{\tau}_{ij}^{-1}$, reduce to:

$$\hat{\tau}_{13}^{-1} = \left(\hat{\tau}_{13} - \frac{\hat{\tau}_{11}\hat{\tau}_{33}}{\hat{\tau}_{13}}\right)^{-1}, \tag{17a}$$

$$\hat{\tau}_{11}^{-1} = \left(\hat{\tau}_{11} - \frac{\hat{\tau}_{13}^2}{\hat{\tau}_{33}}\right)^{-1}, \tag{17b}$$

$$\hat{\tau}_{33}^{-1} = \left(\hat{\tau}_{33} - \frac{\hat{\tau}_{13}^2}{\hat{\tau}_{11}}\right)^{-1}. \tag{17c}$$

With the Eulerian velocity field from the preceding section, and the turbulent fluctuation obtained here, the total velocity in the air can be obtained. The kinematic Reynolds stress tensor field above is the only remaining variable needed for the LS model. However, the turbulent stress in the MBL above a wavy surface is significantly more complicated than that above a flat, rigid surface. The following section briefly summarizes the stress model employed here (Mueller and Veron 2008) and also developed in the context of the stratified MBL for looking at particle turbulent dispersion.

3 Stress in the Wave Boundary Layer

Even though the MBL can be approximated as a constant-stress layer, the presence of waves on a multitude of scales makes the partition of the total stress more complex than the smooth flow case over a flat, rigid plate. As in the familiar flat plate case, there is a viscous sublayer at the surface, where molecular forces are important. Over the ocean, a wave boundary layer (WBL), where momentum is exchanged between the air and sea to form and to sustain waves, also exists at the surface. The height of this layer depends on the wavelength of each individual wave present. Thus, there are a wide range of scales, which can be as small as the order of a few tens of mm for capillary waves and as large as the order of 100 m for surface gravity waves. Before the discussion of the vertical profiles for the individual stress components, the air-sea surface stress must be known.

In addition to the viscous stress component, there is also stress due to the wave-induced momentum flux as well as air-flow separation. Similar to Kudyavtsev and Makin (2007) and Mueller and Veron (2008), the air-sea surface stress can be decomposed as follows:

$$\tau|_{\zeta=0} = \tau_v + \tau_w + \tau_s, \tag{18}$$

where τ_v, τ_w, and τ_s are the viscous, wave-induced, and separation stresses, respectively. The relative importance of each stress component depends upon both the wind speed regime and the sea state. For example, the fraction of the viscous stress compared to the total stress generally decreases as the wind speed increases due to both the additional form drag from a rougher bottom boundary and the sheltering effects of air-flow separation.

The constant-stress layer assumption implies:

$$\tau(\zeta) = \tau(0) = \tau_v(\zeta) + \tau_w(\zeta) + \tau_s(\zeta) + \tau_t(\zeta), \tag{19}$$

with the turbulent stress, τ_t. Although the total stress is conserved, the fraction of each stress component changes substantially within the MBL. Neglecting the contribution from the wave perturbation, the vertical profile of the viscous stress is implicitly defined from the horizontal velocity profile:

$$\tau_v(\zeta) \approx \rho\nu \frac{\partial \overline{U}_1(\zeta)}{\partial \zeta}. \tag{20}$$

Similar to Makin and Kudyavtsev (1999), the wave-induced stress profile becomes:

$$\tau_w(\zeta) = \sum_n \mathrm{d}\tau_w(k_n) \cos\left(\frac{\pi k_n \zeta}{2\delta}\right) \exp\left(-\frac{k_n \zeta}{\delta}\right), \tag{21}$$

where $\mathrm{d}\tau_w(k_n)$ is the wave-induced stress at the surface for each discrete wave mode, n, of wavenumber k_n at the surface, and $\delta \sim 0.1$ is the non-dimensional inner layer thickness (Belcher and Hunt 1993). Though the wave-induced stress profile given in Eq. 21 with $\delta \approx 0.1$ was found to be a fair approximation to, and consistent with, laboratory experiments showing the rapid distortion of turbulence above wind-waves (Mastenbroek et al. 1996), we compare this profile form to the direct numerical simulation (DNS) results over monochromatic waves from Sullivan et al. (2000). Although their DNS results for a solid, moving monochromatic wave are limited to a lower Reynolds number regime than typically found in the MBL, this comparison provides another validation for the wave-induced stress profile. Assuming a monochromatic wave field in Eq. 21 and a wave-induced stress fraction of 0.25 at the surface, Fig. 3a shows the wave-induced stress profile for $\delta = 0.1$ and $\delta = 0.5$. For comparison, the lower wave age ($c/u_* < 8$) results from Sullivan et al. (2000) are also plotted. To compare to the steeper case, $ak = 0.2$ in Sullivan et al. (2000), we take a wave-induced fraction of 0.55 at the surface and $\delta = 0.5$. For the higher end of young wave ages, the use of $\delta = 0.5$ seems more appropriate, independent of the surface fraction of wave-induced stress. But in the limit of stationary hills ($c/u_* = 0$), the theoretical value $\delta = 0.1$ fits the data better. Because the wave-induced stress is carried mostly by the young, short waves (e.g. Mueller and Veron 2008; Makin and Kudyavtsev 1999), we expect the wave ages of these waves to be closer to zero. Therefore, we take $\delta = 0.1$.

Because the local turbulent intensities within the separation bubble are significantly higher than in non-separated regions (e.g. Veron et al. 2007; Reul et al. 2008), the average surface separation stress is assumed to be turbulent stress throughout the boundary layer. Thus, from Eqs. 18, 19, the constant-stress layer assumption yields the following turbulent stress profile:

$$\tau_t(\zeta) = \tau(0) - \tau_v(\zeta) - \tau_w(\zeta). \tag{22}$$

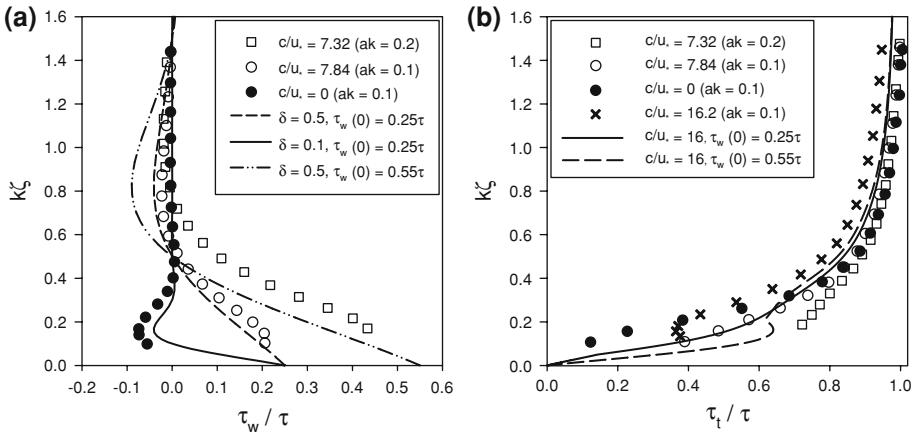

Fig. 3 **a** Fraction of wave-induced stress as a function of wavenumber-normalized height for $\delta = 0.1$ (*solid line*) and $\delta = 0.5$ (*dashed* and *dashed-dotted lines*) along with DNS results of Sullivan et al. (2000) (*symbols*) for rigid, moving waves (*open*) and stationary hills (*closed*). **b** Fraction of turbulent stress as a function of wavenumber-normalized height for wave age $c/u_* = 16$ (*solid* and *dashed line*) along with DNS results of Sullivan et al. (2000) (*symbols*) for moving waves (*open symbols* and *crosses*) and stationary hills (*closed circles*)

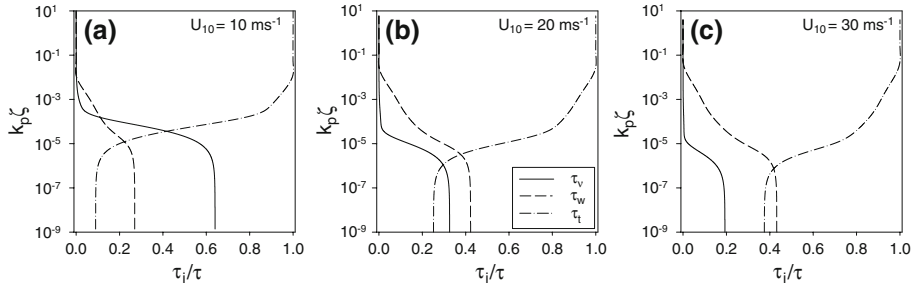

Fig. 4 Vertical profiles of viscous (τ_v), wave-induced (τ_w), and turbulent (τ_t) stress partitions for 10-m wind speeds of $10\,\mathrm{m\,s^{-1}}$ (**a**), $20\,\mathrm{m\,s^{-1}}$ (**b**), and $30\,\mathrm{m\,s^{-1}}$ (**c**)

Figure 4 shows the vertical profiles of the stress components for three different 10-m wind speeds, with dominant wave slopes between 0.10 and 0.16. As the wind speed increases the viscous fraction of the surface stress decreases while the turbulent and wave-induced fractions of the stress increase. The height of the viscous layer, though nearly constant in wall coordinates, decreases with increasing wind speed. The wave boundary layer grows as the waves become larger. Here the height is normalized by the peak wavenumber (0.14, 0.06 and $0.04\,\mathrm{rad\,m^{-1}}$, respectively) such that the increasing thickness of the WBL with wind speed is obscured. Figure 3b compares the fraction of turbulent stress to the DNS results from Sullivan et al. (2000), where we forced our model to match the total surface stress and its fractional components. The wavenumber-normalized height ($k\zeta$) for the wave age of $c/u_* = 16$ happens to scale with the viscous sublayer profile. As noted earlier, the phase speeds in our model are determined by the deep-water dispersion relationship of gravity-capillary waves such that the wavenumber, k, determines the phase speed c. For younger wave ages ($c/u_* < 16$), the wavenumber-normalized height is too large. For older waves ($c/u_* > 16$), the wavenumber-normalized height is too small. Nevertheless, the viscous stress found from the velocity

gradient looks to agree well with the DNS results. Also, Fig. 3b shows that the profile of wave-induced stress from Eq. 21 can produce the type of oscillations seen in the DNS results around the wave age ($c/u_* \approx 16$). Finally, an increased fraction of wave-induced stress seems to shift the turbulent stress profile to the right, consistent with the DNS results in which the turbulent stress profile for the steeper waves, with presumably greater wave-induced stress, is shifted to the right for similar wave age.

With the turbulent stress, the Reynolds stress tensor from the previous section can now be defined as:

$$\hat{\tau}_{11} = \sigma_1^2, \tag{23a}$$

$$\hat{\tau}_{33} = \sigma_3^2, \tag{23b}$$

$$\hat{\tau}_{13} = -\tau_t/\rho, \tag{23c}$$

where the variances of the turbulent velocities in neutral stratification conditions are:

$$\sigma_1^2 = 12^{2/3}\tau_t/\rho, \tag{24a}$$

$$\sigma_3^2 = 1.25^2\tau_t/\rho. \tag{24b}$$

The variances of the turbulent velocities for unstable and stable stratification can be found in Panofsky et al. (1977) and Pahlow et al. (2001), for example. This closes the LS model of fluid particles and fully defines the velocity in the airflow that includes a mean and Lagrangian turbulent fluctuations. In the context of looking at the Lagrangian dispersion of heavy particles, however, the LS model needs to be further extended to non-fluid particles, whose trajectories differ from those of air parcels modelled above.

4 Heavy Particle Motion

With the LS model for a fluid particle given in the preceding sections, we now expand the LS model for a heavy particle. First, we consider the response of the particle to the forcing air flow.

In an unsteady air flow, the linear equation of motion for a spherical particle of radius, r, and density, ρ_p, is (for a full, detailed derivation see Maxey and Riley 1983):

$$\begin{aligned}\left(\frac{4}{3}\pi r^3\rho_p\right)\frac{\mathrm{d}v_i}{\mathrm{d}t} &= \frac{1}{2}\rho C_p A\left(u_i - v_i\right)|\mathbf{u}-\mathbf{v}| + \left(\frac{4}{3}\pi r^3\left(\rho_p-\rho\right)\right)\mathbf{g} \\ &+ \frac{1}{2}\left(\frac{4}{3}\pi r^3\rho\right)\left(\frac{\mathrm{d}u_i}{\mathrm{d}t} - \frac{\mathrm{d}v_i}{\mathrm{d}t}\right) + \left(\frac{4}{3}\pi r^3\rho\right)\frac{du_i}{dt} \\ &+ 6r^2\rho\sqrt{\pi\nu}\int_0^t\left(\frac{\mathrm{d}u_i}{\mathrm{d}\lambda} - \frac{\mathrm{d}v_i}{\mathrm{d}\lambda}\right)\frac{\mathrm{d}\lambda}{\sqrt{t-\lambda}}\end{aligned} \tag{25}$$

where C_p is the drag coefficient on the particle, $A = \pi r^2$ is its cross-section, and $\mathbf{g}$ is the gravitational acceleration vector. As before, the total velocity vector of the air is given by $\mathbf{u}$, while that of the particle is denoted by $\mathbf{v}$. In the equation above, on the right-hand side, the first term is the steady viscous drag on the particle, the second term is the gravity/buoyancy term, the third term is the so-called added-mass, the fourth term accounts for the acceleration from the pressure gradient in the air, and the last term is the Basset history term that accounts for past relative acceleration in an unsteady flow. In practice, a cut-off time limit for the Basset history integration avoids an increasingly expensive calculation for each timestep.

All the terms that are introduced from the unsteadiness of the flow (terms 3–5) are typically neglected in most particle dispersion models because the ratio of the particle density to the air density is large, i.e. $\left(\rho_p/\rho\right) \geq O(10^3)$. While this simplification is valid if the temporal velocity gradients are small, it is inaccurate when these gradients of either the air or the particle are large. These terms are important when, for example, sea-spray droplets are ejected from the water surface and when particles in general fall through the near-surface boundary layer. Our model solves Eq. 25 without further simplification using a fourth-order Runge-Kutta scheme at each timestep. The instantaneous drag coefficient on the particle is obtained from the steady solution (Clift and Gauvin 1970):

$$C_p = \frac{24}{Re_p}\left(1 + 0.15Re_p^{0.687} + \frac{0.0175}{1 + 4.25 \times 10^4 Re_p^{-1.16}}\right), \tag{26}$$

where $Re_p = 2r\left|\mathbf{u} - \mathbf{v}\right|/\nu$ is the instantaneous particle Reynolds number.

While the LS model provides the turbulent velocity following a fluid particle, when following a particle with significant inertia, the new position at each subsequent timestep no longer corresponds to the new position of the fluid particle. Rather, the separation distance between the fluid particle and the heavy particle must be taken into account at each timestep. Intuitively, the correlation of the fluid velocity following a heavy particle should be lower than the correlation following a fluid particle. Sawford and Guest (1991) proposed a reduced Lagrangian time scale, T_L, for the generalized Langevin equation (Eq. 11) when following a particle with significant inertia. For the time scale along a particle's path, Csanady (1963) proposed a simple interpolation between the fluid particle time scale, T_L, and the time scale, L_E/w_t, where L_E and w_t are the Eulerian length scale and terminal velocity of the particle, respectively. Sawford and Guest (1991) extended this parameterization of the time scale along the particle's path to differentiate the longitudinal and transverse directions:

$$T_p = \frac{T_L}{\sqrt{1 + \left(\frac{w_t T_L}{L_E}\right)^2}}, \tag{27}$$

where L_E differs by a factor of 2 between the longitudinal and transverse directions for isotropic turbulence (Tennekes and Lumley 1972). There are two limitations of this model that makes it unsuitable for the MBL. First, the particle is assumed to be travelling vertically at its terminal velocity. Due to wave-induced and turbulent motions, even heavy particles are not necessarily travelling at their terminal velocity. Second, this parameterization does not account for the anisotropic case, in which the longitudinal and transverse Eulerian length scales are different in each direction.

Zhuang et al. (1989) proposed a slightly different approach. They accounted for the separation between the fluid particle trajectory and the heavy particle trajectory explicitly in their autocorrelation coefficient as follows:

$$\tilde{R} = \exp\left(-\Delta t/T_L - \left|\mathbf{s}\right|/L_E\right), \tag{28}$$

where $\mathbf{s}$ is the separation vector between the fluid particle trajectory and the heavy particle trajectory. They too included a distinction between the Eulerian length scales but did not extend their model to the anisotropic case. Another setback of their model is that in addition to tracking the separation between the fluid and heavy particle trajectories at the previous timestep, their model also tracks the original fluid eddy until the total separation between the heavy particle and the fluid particle is greater than the eddy length scale. Once the total

separation becomes larger, a new eddy begins, and the tracking of both trajectories resumes. This extra feature nearly doubles the computational cost for each heavy particle simulation.

We propose a formulation that not only tracks the separation at each timestep explicitly but also extends to the anisotropic case that is necessary to properly model the stratified MBL. If the longitudinal, L_f, and transverse, L_g, Eulerian length scales differ in the horizontal and vertical directions, there are four length scales:

$$L_{fi} = \frac{\sigma_i^3}{2\varepsilon}, \tag{29a}$$

$$L_{gi} = \frac{\sigma_i^3}{4\varepsilon}, \tag{29b}$$

with $i = \{1,\ 3\}$. Similar to Zhuang et al. (1989), the resulting two autocorrelation coefficients include both the Lagrangian time scale and Eulerian length scales as:

$$\hat{R}_1 = \exp\left[-\frac{\Delta t}{T_{L_1}} - \left(\frac{|s_1|}{L_{f_1}}\right)^{\frac{2}{3}} - \left(\frac{|s_3|}{L_{g_3}}\right)^{\frac{2}{3}}\right], \tag{30a}$$

$$\hat{R}_3 = \exp\left[-\frac{\Delta t}{T_{L_3}} - \left(\frac{|s_3|}{L_{f_3}}\right)^{\frac{2}{3}} - \left(\frac{|s_1|}{L_{g_1}}\right)^{\frac{2}{3}}\right]. \tag{30b}$$

Our model differentiates the direction of the separation between the fluid particle and heavy particle at each timestep and calculates the decorrelation accordingly. Our model does not, however, track the original fluid eddy particle as Zhuang et al. (1989). Also, the exponent for the separation between the fluid particle and the heavy particle is 2/3, as given by the Eulerian structure function, instead of 1. The autocorrelation function (Eq. 30) satisfies the limits of an extremely heavy particle falling through the eddies and a massless fluid particle following the eddies. Noting that $\mathrm{d}x_i/\mathrm{d}t = u_i$, our parameterization can be expressed in a form similar to Csanady's parameterization:

$$T_{p_1}^H = \frac{T_{L_1}^H}{1 + T_{L_1}^H\left[\left(\frac{|u_1 - v_1|}{L_{f_1}}\right)^H + \left(\frac{|u_3 - v_3|}{L_{g_3}}\right)^H\right]}, \tag{31a}$$

$$T_{p_3}^H = \frac{T_{L_3}^H}{1 + T_{L_3}^H\left[\left(\frac{|u_3 - v_3|}{L_{f_3}}\right)^H + \left(\frac{|u_1 - v_1|}{L_{g_1}}\right)^H\right]} \tag{31b}$$

where the exponent H is 1 or 2/3 for the fluid particle or extreme heavy particle limits, respectively. Zhuang et al. (1989), Csanady (1963) and Sawford and Guest (1991) assumed $H = 1$. While this is correct for the fluid particle limit, it does not strictly satisfy the Eulerian structure function. Moreover, Csanady (1963) and Sawford and Guest (1991) took the denominator to be the Euclidean norm interpolation of the two terms in the denominator, with the slip velocity equal to the particle terminal velocity as in Eq. 27. When $H = 2/3$, the Langevin equation is fractional (i.e., $\Delta t^{2/3}$), and thus the Lagrangian structure function is no longer satisfied. Reynolds and Cohen (2002) explore this space-time conundrum in more detail and offer yet another formulation. With tuning, all of these models provide fair agreement with the data from Snyder and Lumley (1971). We also note that within the limits of their experimental scatter, the shapes of both the particle velocity autocorrelation and the Eulerian spatial correlation were similar. This implies that, in practice, the assumption that $H = 1$ may not be entirely problematic. Nevertheless, our approach, (Eq. 30 in Eq. 16),

satisfies the Lagrangian and Eulerian structure functions in the two limits, includes the effect of anisotropy and accounts for the slip velocity between the air and particle explicitly rather than assuming the slip velocity always equals the terminal velocity.

5 Results

Over a flat, rigid boundary, Kolmogorov's similarity theory, K41 (Kolmogorov 1941, 1962), yields the following Lagrangian time spectrum within the inertial subrange (Inoue 1952; Corrsin 1963):

$$E(f) = \pi^{-1} C_0 \varepsilon f^{-2}. \tag{32}$$

Below the inertial subrange, the spectrum is white. At frequencies higher than some frequency (here assumed to be $f = 0.74\tau_K^{-1}$, where τ_K is the temporal Kolmogorov microscale) within the dissipative range, the spectrum falls off rapidly. We have run the model for a fluid particle initially placed at 1 m above the surface in a 15 m s^{-1} wind speed and tracked it as it propagates through the MBL. The height of this particular particle never exceeded 30 m above the surface. Figure 5 shows the spectrum of the vertical velocity of the fluid particle. For comparison, a line proportional to the spectrum expected over a flat, rigid boundary is also provided; the theoretical inertial subrange lies between the vertical dashed lines. As the particle traverses the MBL and changes height above the surface, the turbulent intensity and the viscous dissipation rate changes because they vary vertically in space as do the turbulent stresses (Sect. 3). For the purpose of this comparison and for the results plotted on Fig. 5, we take the mean dissipation rate and turbulent intensity as experienced by the fluid particle as it traverses the MBL. Of course, one advantage of this Lagrangian approach is the ability to follow the heavy particle as it traverses the MBL, which enables a local estimation of the stress, dissipation rate and other parameters used to solve the particle momentum, heat and mass (if necessary) equations. The spectrum generally follows the expected spectrum over a flat boundary but appears to be slightly higher, which could be due, in this wavy surface case, to the estimation of the dissipation rate shown in Appendix B. More likely, this could also be due to the use of mean values to scale the spectrum. Nevertheless, the fluid parcel spectrum still follows the expected K41 frequency dependence throughout most of the inertial

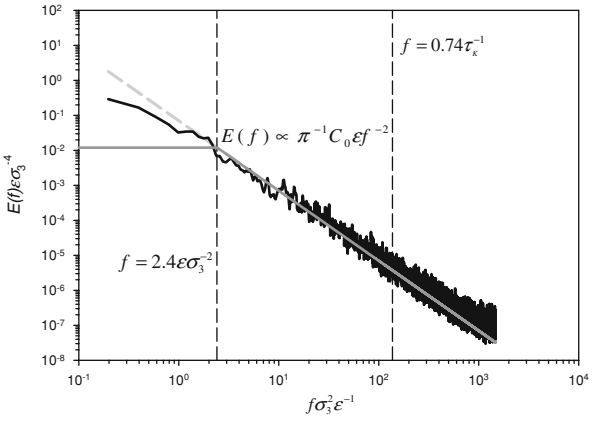

Fig. 5 Spectrum of carrier fluid vertical velocity following a fluid parcel (*black*) and the theoretical spectrum (*grey*)

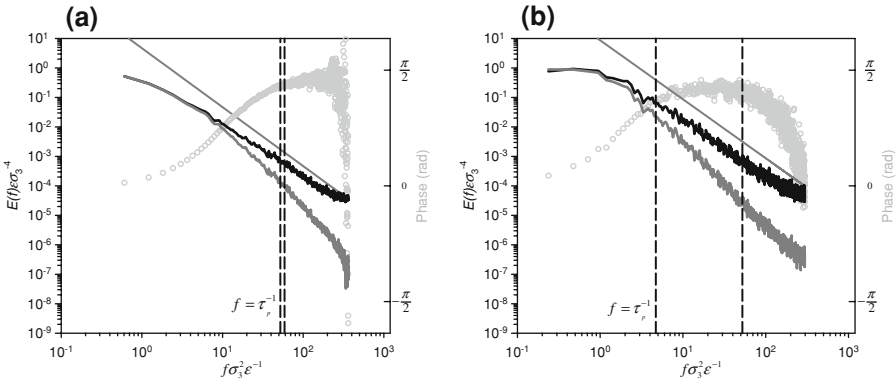

Fig. 6 The vertical velocity spectra of the *air* following the particle (*black*) and the particle itself (*grey*) for a 10-μm radius lead particle (**a**) and a 100-μm radius water sphere (**b**) along with the theoretical f^{-2} relationship (*dark grey line*), the particle response frequency (*first dashed line*), the beginning of the dissipation range (*second dashed line*), and the phase relationship between the air and particle (*grey circles*)

subrange, as Fig. 5 illustrates. At the other end, the spectrum continues into the dissipation range due to the timestep requirements to ensure all terms in the exponent of Eq. 30 are small. Although this high frequency fluctuation is not physical, for practical purposes there are no adverse consequences to using timesteps smaller than the temporal Kolmogorov microscale (Wilson and Zhuang 1989).

In addition, to illustrate the behaviour of the model with heavy, non-fluid particles, we have tracked two different heavy particles, a lead particle and a water droplet, as they are transported through the MBL. Unlike fluid particles, heavy particles take a finite amount of time to adjust to the ambient air flow, which is approximately the Stokes' response time[1]:

$$\tau_p = \frac{2\rho_p r^2}{9\mu}, \tag{33}$$

where μ is the dynamic viscosity of the carrier fluid. Figure 6a shows the vertical velocity spectrum of a lead particle with 10-μm radius along with that of the air following the particle. For reference, the inverse response time (left, vertical dashed line), the theoretical cut-off frequency (right, vertical dashed line), and the f^{-2} relationship are also plotted. The lead particle has sufficient inertia such that it does not follow the air flow. Consequently, the spectrum of the air flow following the lead particle is somewhat flatter than that shown for a fluid particle in Fig. 5. This is due to the decorrelation from the spatial separation between the fluid and the heavy particle trajectories. At frequencies much lower than the inverse

[1] Assuming that the particle response time is given by the Stokes' time scale is in fact assuming that the equation of motion is dominated by the first two terms on the right-hand side of Eq. 25 and the drag coefficient satisfies the low-Reynolds number limit of Stokes' flow. This is generally valid in the case presented here but will not necessarily be valid throughout the MBL, specifically in regions where wind speeds and other turbulent parameters vary significantly (e.g. near the molecular layer). Nonetheless, our model remains valid even in those regions where the particle response time will be different from the Stokes time scale given by Eq. 33. Again, this emphasizes the advantage of the Lagrangian approach where local parameters, rather than averaged ones, are used to estimate the local, instantaneous response of the particles.

response time, the lead particle follows the air flow exactly because there is sufficient time for the particle to adjust to the flow. At higher frequencies, the particle departs from the f^{-2} regime of the air flow and undergoes a transition to a f^{-4} regime, as expected. The phase relationship between the air following the lead particle and the lead particle itself illustrates these two regimes further. At low frequencies, the particle and air are in phase, while at higher frequencies, the air and particle are fully out of phase ($\pi/2$). Furthermore, at the highest frequencies the heavy particle displacement, **s**, dominates the correlation function, and thus, the spectrum of the air following the particle flattens out and the phase relationship scatters. The characteristic particle Reynolds number for this simulation is $Re_p \approx 0.4$ with a maximum instantaneous value of 4. Figure 6b shows the vertical velocity spectrum of a water sphere with 100-μm radius along with that of the air following the water sphere. This particle is sufficiently heavy that, for most frequencies, the particle departs from the air flow. Its significant separation from the air flow also adds to the spectrum at the highest frequencies, but once again, due to timestep requirements, there are unphysical fluctuations at frequencies well into the dissipation range. The characteristic particle Reynolds number, $Re_p \approx 12$, and maximum instantaneous value, 52, are somewhat higher than for the lead particle. This difference is due to their relative radii sizes in addition to their relative slip velocity magnitudes. Finally, the phase relationship at the highest frequencies tends to a wide range centered near zero. Although the particle response time is much larger than the shortest time scale where this relationship occurs, the relative location of the temporal Kolmogorov microscale prohibits any robust, physical interpretation.

6 Conclusion

We have developed a LS model for heavy particles in the MBL where the turbulent stresses change with height above the wavy water surface. In addition to a model for these turbulent stresses, the traditional particle correlation function has been extended to the anisotropic, unsteady case. The turbulent motion of a fluid particle in a Lagrangian frame of reference is characteristically similar in the MBL, that is, the velocity spectrum still follows rather closely to the predicted K41 behaviour with a f^{-2} dependence. The difference in the MBL is perhaps a consequence of the wave-induced contribution to the local dissipation of energy, but the necessity to scale with the mean turbulent intensity and dissipation rate obscures this conclusion. When following a heavy particle, however, the velocity spectrum of the air at the location of the particle no longer follows the theoretical slope. Instead, the actual spectral slope is shallower due to additional decorrelation from the separation between the fluid flow and the particle trajectory. The spectrum of the particle velocity follows the air spectrum until roughly the frequency corresponding to the inverse particle response time. Beyond that frequency, the particle velocity spectrum undergoes a transition to a steeper slope, which roughly exhibits a f^{-4} dependence. The phase relationship between a heavy particle and the velocities of the surrounding air flow changes from being in phase to completely out of phase, as expected from the equation of motion where the dominant terms are drag and buoyancy. We conclude that this improved LS model will prove useful in the modelling of sea-spray dispersion above the wavy water surface in which case the lower atmospheric layers are expected to be significantly stratified. The Lagrangian approach simplifies the estimation of momentum, latent heat, and sensible heat fluxes from the droplets and yields accurate flight times and trajectories, which will in turn lead to an accurate estimate of the overall spray-mediated air-sea fluxes.

Acknowldegment This work was supported by the Office of Naval Research (ONR) under grant N00014-05-1-0609 to Veron.

Appendix

A Bulk Conservation of Mass

In Sect. 2.1, the vertical profile of the mean horizontal velocity follows the wavy surface. Without further modification, the vertical integral of the mean horizontal velocity from the surface upward would not remain constant. Fortunately, the amount of horizontal flux lost/gained is merely a function of the deviation of the surface from the mean water level. Due to the deviation from the mean water level, η, the extra or missing vertically integrated horizontal flux is:

$$M_F(\eta) = -\eta \overline{U}_1(\infty) \approx -\eta \overline{U}_1(10). \tag{34}$$

To maintain a constant mass flux, we modify the flow $\overline{U}_1$ by adding U_1^{acc}, where $\int U_1^{acc} = -M_F$, and thus ensuring:

$$\int_0^\infty \left(\overline{U}_1 + U_1^{acc}\right) \mathrm{d}\zeta = \int_0^\infty \overline{U}_1 \mathrm{d}\zeta - M_F = const. \tag{35}$$

In other words, the acceleration and deceleration of the air flow, U_1^{acc}, allows for the mass flux to be conserved. This compression and expansion of the profile should asymptote to zero at infinite height, while also tending to zero at the surface. As before, the vertical profile of the horizontal acceleration velocity is damped with height relative to the wavenumber of the nth wave mode:

$$\begin{aligned} U_1^{acc}(x,\zeta,t) = \overline{U}_1(10) &\left(1 - \exp\left(-\frac{u_{*_\nu}\zeta}{5\nu}\right)\right) \\ &\times \sum_n \left(k_n + \frac{5k_n^2\nu}{u_{*_\nu}}\right) a_n \exp\left(-k_n\zeta\right). \end{aligned} \tag{36}$$

The exponential expressions maintain the proper lower and upper boundary conditions given above, and the $k+5k^2\nu/u_{*_\nu}$ expression ensures $\int_0^\infty U_1^{acc}\mathrm{d}\zeta = -M_F$ with these two damping terms. The vertical component is found as before (Eq. 6):

$$U_3^{acc} = U_1^{acc}\alpha. \tag{37}$$

Thus, the wave-phase-dependent horizontal and vertical velocities become $\widetilde{u}_1 = U_1^{orb} + U_1^{acc}$ and $\widetilde{u}_3 = U_3^{sur} + U_3^{orb} + U_3^{acc}$, respectively. The large-scale horizontal flux is conserved, and the local divergence of the velocity field is zero to first order in the wave slope.

B Bulk Conservation of Energy

From Hara and Belcher (2004), the total energy budget in the wave boundary layer is:

$$\frac{\mathrm{d}}{\mathrm{d}\zeta}(\overline{U}\tau) + B_P + \frac{\mathrm{d}\Pi}{\mathrm{d}\zeta} + \frac{\mathrm{d}\Pi'}{\mathrm{d}\zeta} - \rho\varepsilon = 0, \tag{38}$$

where Π and Π' are the vertical transport of wave-induced motions and turbulent kinetic energy (TKE), respectively, and B_P is buoyancy production due to stratification. Assuming a constant-stress layer, the viscous dissipation rate, ε, can be determined from the *bulk conservation of energy* as:

$$\rho\varepsilon = (\tau_w + \tau_t)\frac{\mathrm{d}\overline{U}}{\mathrm{d}\zeta} + B_P + \frac{\mathrm{d}\Pi}{\mathrm{d}\zeta}, \tag{39}$$

where $\mathrm{d}\Pi/\mathrm{d}\zeta$ is the divergence of the wave-induced energy flux. Assuming pressure transport is the largest contribution to Π, the vertical transport of wave-induced motions is:

$$\Pi(\zeta) = \int c(k)\mathrm{d}\tau_w(\zeta, k), \tag{40}$$

where $\mathrm{d}\tau_w$ is the spectral density of wave-induced stress. Because the velocity profile is assumed to be in the form of Eq. 4, the dissipation rate is fully defined. This approach is different from that in Hara and Belcher (2004), where the velocity profile includes the WBL profile derived from both the conservation of energy and the defined form of the dissipation rate.

References

Belcher SE, Hunt JCR (1993) Turbulent shear flow over slowly moving waves. J Fluid Mech 251:119–148

Brickman D, Smith PC (2002) Lagrangian stochastic modeling in coastal oceanography. J Atmos Ocean Technol 19:83–99

Clift R, Gauvin WH (1970) The motion of particles in turbulent gas streams. Proc Chemeca 70(1):14–28

Corrsin S (1963) Estimates of the relations between Eulerian and Lagrangian scales in large Reynolds number turbulence. J Atmos Sci 20:115–119

Csanady GT (1963) Turbulent diffusion of heavy particles in the atmosphere. J Atmos Sci 20:201–208

Du S, Sawford BL, Wilson JD, Wilson DJ (1995) Estimation of the Kolmogorov constant (C_0) for the Lagrangian structure function, using a second-order Lagrangian stochastic model of grid turbulence. Phys Fluids 7:3083–3090

Elfouhaily T, Chapron B, Katsaros K, Vandemark D (1997) A unified directional spectrum for long and short wind-driven waves. J Geophys Res 102:15781–15796

Hara T, Belcher SE (2004) Wind profile and drag coefficient over mature ocean surface wave spectra. J Phys Ocean 34:2345–2358

Inoue E (1952) On the Lagrangian correlation coefficient of turbulent diffusion and its application to atmospheric diffusion phenomena. Geophys Res Paper No 19:397–412

Kolmogorov AN (1941) The local structure of turbulence in incompressible viscous fluid for very large Reynolds numbers. CR Dokl Acad Sci URSS 30:301–305

Kolmogorov AN (1962) A refinement of previous hypotheses concerning the local structure of turbulence in a viscous incompressible fluid at high Reynolds number. J Fluid Mech 13:82–85

Kudryavtsev VN, Makin VK (2007) Aerodynamic roughness of the sea surface at high winds. Boundary-Layer Meteorol 125:289–303

Makin VK, Kudryavtsev VN (1999) Coupled sea surface-atmosphere model 1. Wind over waves coupling. J Geophys Res 104:7613–7624

Mastenbroek C, Makin VK, Garat MH, Giovanangeli JP (1996) Experimental evidence of the rapid distortion of turbulence in the air flow over water waves. J Fluid Mech 318:273–302

Maxey MR, Riley JJ (1983) Equation of motion for a small rigid sphere in a nonuniform flow. Phys Fluids 26:883–889

Mueller JA, Veron F (2008) Nonlinear formulation of the bulk surface stress over breaking waves: feedback mechanisms from air-flow separation. Boundary-Layer Meteorol. doi:10.1007/s10546-008-9334-6

Pahlow M, Parlange M, Port-Agel F (2001) On Monin-Obukhov similarity in the stable atmospheric boundary layer. Boundary-Layer Meteorol 99:225–248

Panofsky H, Tennekes H, Lenschow D, Wyngaard J (1977) The characteristics of turbulent velocity components in the surface layer under convective conditions. Boundary-Layer Meteorol 11:355–361

Reeks MW (1977) On the dispersion of small particles suspended in an isotropic turbulent fluid. J Fluid Mech 83:529–546
Reul N, Branger H, Giovanangeli J-P (2008) Air flow structure over short-gravity breaking water waves. Boundary-Layer Meteorol 126:477–505
Reynolds AM, Cohen JE (2002) Stochastic simulation of heavy-particle trajectories in turbulent flows. Phys Fluids 14:342–351
Rodean HC (1996) Stochastic Lagrangian models of turbulent diffusion. American Meteorology Society, Boston, 84 pp
Sawford BL, Guest FM (1991) Lagrangian statistical simulations of the turbulent motion of heavy particles. Boundary-Layer Meteorol 54:147–166
Snyder WH, Lumley JL (1971) Some measurements of particle velocity autocorrelation functions in a turbulent flow. J Fluid Mech 48:41–71
Sullivan PP, McWilliams JC, Moeng CH (2000) Simulation of turbulent flow over idealized water waves. J Fluid Mech 404:47–85. doi:10.1017/S0022112099006965
Taylor GI (1921) Diffusion by continuous movements. Proc Lond Math Soc Ser 2 20:196–212
Tennekes H, Lumley JL (1972) A first course in turbulence. MIT Press, London, 300 pp
Thomson DJ (1987) Criteria for the selection of stochastic models of particle trajectories in turbulent flows. J Fluid Mech 180:529–556
Veron F, Saxena G, Misra SK (2007) Measurements of the viscous tangential stress in the airflow above wind waves. Geophys Res Lett 34:L19603. doi:10.1029/2007GL031242
Wang L-P, Maxey MR (1993) Settling velocity and concentration distribution of heavy particles in homogeneous isotropic turbulence. J Fluid Mech 256:27–68
Webb EK (1982) On the correction of flux measurements for effects of heat and water vapour transfer. Boundary-Layer Meteorol 23:251–254
Webb EK, Pearman GI, Leuning R (1980) Correction of flux measurements for density effects due to heat and water vapour transfer. Q J R Meteorol Society 106:85–100
Weil JC, Sullivan PP, Moeng C-H (2004) The use of large-eddy simulations in Lagrangian particle dispersion models. J Atmos Sci 61:2877–2887
Wells MR, Stock DE (1983) The effects of crossing trajectories on the dispersion of particles in a turbulent flow. J Fluid Mech 136:31–62
Wilson JD (2000) Trajectory models for heavy particles in atmospheric turbulence: comparison with observations. J Appl Meteorol 39:1894–1912
Wilson JD, Sawford BL (1996) Review of Lagrangian stochastic models for trajectories in the turbulent atmosphere. Boundary-Layer Meteorol 78:191–210
Wilson JD, Zhuang Y (1989) Restriction on the timestep to be used in stochastic Lagrangian models of turbulent dispersion. Boundary-Layer Meteorol 49:309–316
Wu J (1983) Sea-surface drift currents induced by wind and waves. J Phys Oceanogr 13:1441–1451
Yeung PK (2002) Lagrangian investigations of turbulence. Annu Rev Fluid Mech 34:115–142
Yudine MI (1959) Physical considerations on heavy particle diffusion. Adv Geophys 6:185–191
Zhuang Y, Wilson JD, Lozowski EP (1989) A trajectory-simulation model for heavy particle motion in turbulent flow. J Fluids Eng 111:492–494